

Ultralow Impedance Graphene Microelectrodes with High Optical Transparency for Simultaneous Deep Two-Photon Imaging in Transgenic Mice

Yichen Lu, Xin Liu, Ryoma Hattori, Chi Ren, Xingwang Zhang, Takaki Komiyama, and Duygu Kuzum*

The last decades have witnessed substantial progress in optical technologies revolutionizing our ability to record and manipulate neural activity in genetically modified animal models. Meanwhile, human studies mostly rely on electrophysiological recordings of cortical potentials, which cannot be inferred from optical recordings, leading to a gap between our understanding of dynamics of microscale populations and brain-scale neural activity. By enabling concurrent integration of electrical and optical modalities, transparent graphene microelectrodes can close this gap. However, the high impedance of graphene constitutes a big challenge toward the widespread use of this technology. Here, it is experimentally demonstrated that this high impedance of graphene microelectrodes is fundamentally limited by quantum capacitance. This quantum capacitance limit is overcome by creating a parallel conduction path using platinum nanoparticles. A 100 times reduction in graphene electrode impedance is achieved, while maintaining the high optical transparency crucial for deep two-photon microscopy. Using a transgenic mouse model, simultaneous electrical recording of cortical activity with high fidelity is demonstrated while imaging calcium signals at various cortical depths right beneath the transparent microelectrodes. Multimodal analysis of Ca^{2+} spikes and cortical surface potentials offers unique opportunities to bridge our understanding of cellular dynamics and brain-scale neural activity.

1. Introduction

Electrophysiology has been the backbone of neuroscience research for decades.^[1] Despite many advantages, it is often difficult to record from large number of neurons (≈ 1000 cells) simultaneously and from large areas across different brain regions. Last decades have witnessed rapid advancements in optical imaging, such as two-photon calcium imaging, for monitoring hundreds of cells in neuronal microcircuits.^[2] However, slow kinetics of indicators and low frame acquisition rates of typical imaging setups substantially limit the maximum temporal resolution that can be achieved using optical imaging.^[3] Furthermore, neuronal populations display emergent features such as oscillations, waves, synchrony, and sequential activation patterns, which have been historically used as the basis of electrocorticography (ECoG) recordings in clinical studies with human patients. Linking these macroscale features to activities of individual neurons and global effects of these features on the brain activity remain elusive due to the lack of

technologies permitting concurrent cellular-scale recordings and whole brain activity monitoring.

To this end, transparent graphene electrodes have recently been suggested to enable integration of electrophysiology with optical imaging techniques in multimodal experiments.^[4] Owing to unique combination of properties including high mobility, low noise, flexibility and optical transparency, graphene has been intensively investigated for electronics^[5] and sensing applications.^[6] On the other hand, for neural recordings, the impedance of graphene microelectrodes has been relatively high impacting sensitivity of measurements and wide-spread adaptation of the technology for various basic neuroscience and medical applications. Furthermore, high impedance of monolayer graphene constitutes a fundamental roadblock toward scaling graphene microelectrode dimensions to record single neuron activity. In addition, it constitutes a big challenge toward use of graphene electrodes for electrical stimulation in future. Chemical doping techniques have been

Y. Lu, X. Liu, Prof. D. Kuzum
Electrical and Computer Engineering Department
Jacobs School of Engineering
University of California
San Diego 9500 Gilman Drive, La Jolla, CA 92093, USA
E-mail: dkuzum@eng.ucsd.edu

Dr. R. Hattori, C. Ren, Prof. T. Komiyama
Neurobiology Section
Center for Neural Circuits and Behavior
Department of Neurosciences
University of California
San Diego 9500 Gilman Drive, La Jolla, CA 92093, USA

Dr. X. Zhang
Nanoengineering Department
Jacobs School of Engineering
University of California
San Diego 9500 Gilman Drive, La Jolla, CA 92093, USA

 The ORCID identification number(s) for the author(s) of this article can be found under <https://doi.org/10.1002/adfm.201800002>.

DOI: 10.1002/adfm.201800002

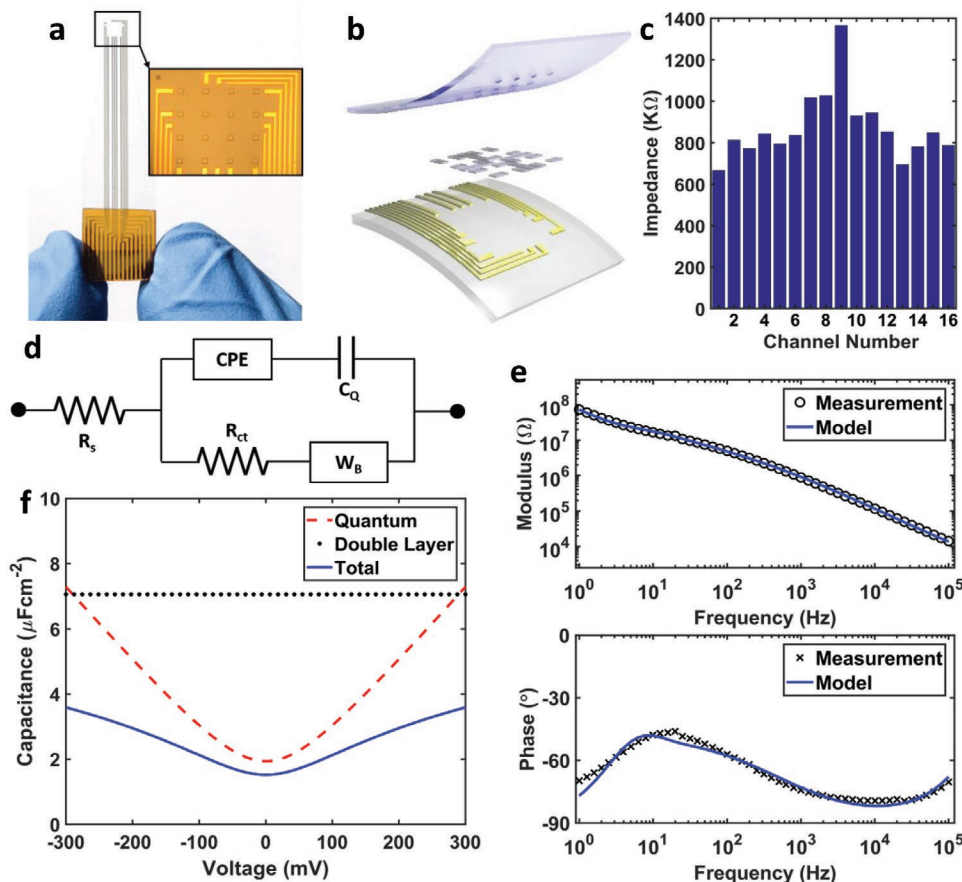


Figure 1. Transparent graphene microelectrode array. a) A photo of the array. The inset is a microscopic image of the 4-by-4 array of the SU-8 openings. b) Schematic shows three layers of the array. The top layer is SU-8 encapsulation, the bottom layer is PET substrate with metal wires and contact pads, and the layer in between is monolayer graphene. c) The electrochemical impedance at 1 KHz of 16 channels in an array, and the average impedance is 872.9 K Ω . d) The equivalent circuit model of graphene electrodes. CPE stands for constant phase element simulating the Helmholtz double-layer capacitance, C_Q is the quantum capacitance, R_{ct} is the charge-transfer resistance, and W_B is the bounded Warburg element simulating diffusion at the interface. e) EIS measurements and the equivalent circuit model fitting of a representative graphene electrode channel are plotted. f) The quantum capacitance, the Helmholtz double capacitance, and the total capacitance with respect to voltage are plotted. The quantum capacitance dominates the capacitive branch from -100 to 100 mV, which is the range of the open-circuit potential of graphene.

shown to reduce the impedance of monolayer graphene to some extent.^[7] However, the decrease in impedance is not sufficient to scale electrode dimensions to single-cell regime. In addition, other techniques such as deposition of porous films or multilayer graphene flakes cannot be employed since they penalize the optical transparency. Transparent materials, such as indium tin oxide (ITO) have also been investigated as the electrode material for transparent microelectrode arrays.^[8] However, ITO is brittle; though widely employed in solar cells and display panels, it is susceptible to cracking and mechanical degradation when used for flexible neural interfaces.^[4b,8] Here we show that the impedance of the graphene electrodes is fundamentally limited by quantum capacitance, which originates from the graphene's low density of states around Dirac point.^[9] We report an effective method to electrodeposit platinum nanoparticles (PtNPs) on transparent chemical vapor deposited (CVD) graphene electrodes to beat the quantum capacitance limit and lower the impedance 100 times while maintaining optical transparency. Employing electrochemical impedance analysis and equivalent circuit modeling, we explain how

electrodeposited PtNPs can overcome the quantum capacitance limit and decrease the impedance. PtNPs do not impede the transparency of neural electrodes or obstruct delivery of light to deeper layers in the tissue. Using graphene/PtNP microelectrode arrays, we demonstrate simultaneous *in vivo* calcium imaging of cellular activity at multiple cortical depths while recording field potentials generated by neural populations from the cortical surface. Multimodal analysis of Ca^{2+} spikes and cortical surface potentials suggest that somatic Ca^{2+} activity in layer II/III significantly contributes to high frequency gamma band for the surface potentials, while the dendritic Ca^{2+} activity from layer I increases the power in low frequency bands.

2. Result and Discussion

2.1. Quantum Capacitance Limit for Graphene Microelectrodes

In this work, we first fabricated graphene microelectrode arrays with $100 \mu\text{m}$ electrode size and $400 \mu\text{m}$ spacing (Figure 1a).

10 nm chromium and 100 nm gold were deposited on to polyethylene terephthalate (PET) substrate to form the metal wires and the contact pads. Preventing crack formation during graphene transfer and protecting graphene surface from chemical contamination are particularly important to achieve high yield in large area transparent arrays. To that end, we used the “bubbling” transfer method^[10] and AZ1512/PMGI bilayer lithography. Graphene pads were then patterned with oxygen plasma etching. And finally, the SU-8 encapsulation layer was defined with photolithography. Details of the fabrication process are described in the Experimental Section and Figure S1 (Supporting Information). Figure 1b displays the trilayer structure of the array, where CVD graphene lays between PET substrate and SU-8 encapsulation. Scanning electron microscopy images (Figure S2, Supporting Information) show that SU-8 encapsulation was well defined by photolithography (no cracks) and the graphene surface has no obvious polymer residue. The graphene/electrolyte interface was then characterized with electrochemical impedance spectroscopy (EIS) and cyclic voltammetry (CV) in 0.01 M phosphate buffered saline (PBS).^[11] EIS was measured at the open-circuit potential of the graphene/PBS interface from 1 Hz to 100 KHz (Figure S3a, Supporting Information). Impedance distribution of a representative array measured at 1 KHz is shown in Figure 1c, the average impedance is 872.9 KΩ. Electrodes with impedances lower than 1.5 MΩ can record neural activity with high signal-to-noise ratio, and those with impedance from 1.5 to 3.0 MΩ might still get acceptable signals.^[12] Our fabrication process provides 100% yield with all the electrodes in the array exhibiting impedances less than 1.5 MΩ CV measured from −0.6 to 1.1 V (Figure S3b, Supporting Information) shows the capacitive characteristics of the graphene interface with no redox peaks, indicating that no Faradaic reactions take place at the interface.

We investigated the origin of high impedance of the graphene microelectrodes by equivalent circuit analysis (Figure 1d). The unique band structure of graphene gives rise to quantum capacitance (C_Q), which is used to describe the total charge ($Q = q(p - n)$ where q is the electron charge) as a function of electrostatic potential.^[9] C_Q around Dirac point is small due to low density of states. Therefore, conventional equivalent circuit models, such as Randles cell used for metal microelectrodes cannot be directly applied to the graphene electrodes. We modified the equivalent circuit model for transparent graphene electrodes to include the quantum capacitance effect (Figure 1d). In the equivalent circuit model, R_s is the resistance of the solution, CPE is the constant phase element representing Helmholtz double-layer capacitance,^[11] W_B is the bounded Warburg element used to simulate the diffusion process, and R_{ct} is the charge-transfer resistance used to simulate Faradaic reactions. Quantum capacitance of graphene (C_Q) is in series with the CPE. Experimental EIS curves and the fitted equivalent circuit model are plotted in Figure 1e. The parameters for the equivalent circuit model are listed in **Table 1** including mean values and standard deviations (SD), and the corresponding formulae in Note S1 (Supporting Information). The quantum capacitance of graphene is measured as 2.45 $\mu\text{F cm}^{-2}$, consistent with experimental and theoretical results in literature.^[13]

Table 1. Means and standard deviations (SD) of parameters in the equivalent circuit model.

	R_s [KΩ]	C_{dl} [$\mu\text{F cm}^{-2}$]	A	W [$\text{M}\Omega \text{ s}^{-1/2}$]	B [$\text{s}^{1/2}$]	R_{ct} [MΩ]	C_Q [$\mu\text{F cm}^{-2}$]
Mean	4.32	7.07	0.924	158	0.333	1.62	2.45
SD	0.29	0.21	3.4×10^{-3}	2.0	3.7×10^{-4}	0.16	4.5×10^{-2}

The effect of quantum capacitance on the total capacitance is shown in Figure 1f. The Helmholtz double layer capacitance is obtained directly from the fitting result. The quantum capacitance is simulated using Equation (1),^[13c] where $v_F \sim c/300$ for graphene, and impurity concentration n^* is estimated to be 10^{12} cm^{-2} to match the fitting result. As the open circuit potential of graphene electrodes typically lies within −100 to 100 mV, quantum capacitance dominates the total capacitance in this region,^[14] decreasing the total capacitance and giving rise to high impedance for the graphene microelectrodes

$$C_Q = \frac{2e^2}{\hbar v_F \sqrt{\pi}} \left(\left(\frac{eV}{\hbar v_F \sqrt{\pi}} \right)^2 + |n^*| \right)^{1/2} \quad (1)$$

2.2. Overcoming Quantum Capacitance Limit

Introducing dopants by chemical means can increase the quantum capacitance slightly and lead to up to twofold decrease in electrochemical impedance.^[7] However, much larger reductions in impedance cannot be achieved by chemical doping since it only shifts Fermi level slightly away from the Dirac point, and hence the quantum capacitance still dominates the electrochemical characteristics of the interface. Here we propose to overcome quantum capacitance limit of transparent graphene electrodes by creating an alternative conduction path with redox catalysts at the electrode/electrolyte interface. Deposition of PtNPs on reduced graphene oxide (RGO),^[15] functionalized graphene sheet,^[16] glassy carbon (GC),^[17] and graphene/glassy carbon bilayer substrate^[18] have been shown to be a compelling approach to boost electroactivity in fuel cell and biochemical sensor applications. In a previous study, platinum, gold, and gold–platinum alloy nanoparticles as electrochemical catalysts. PtNPs demonstrated stronger faradaic reaction and pseudo-capacitance than the gold and gold–platinum alloy counterparts, which make PtNPs the best choice for catalysis.^[15b] However, for those applications, optical transparency was not a requirement. Boosting electroactivity of monolayer graphene while maintaining transparency is yet to be demonstrated. Here we developed a process for electrodeposition of Pt nanoparticles (PtNPs) on monolayer CVD graphene as follows. In a two-electrode cell configuration, the graphene array was connected to the working electrode, and a Pt wire (gauge 25) to the auxiliary electrode (Figure S4, Supporting Information). Both electrodes are immersed into $5 \times 10^{-3} \text{ M H}_2\text{PtCl}_6$ and $10 \times 10^{-3} \text{ M K}_2\text{HPO}_4$ solution. A current of 500 nA was flown out from the graphene array for multiple time periods (5, 10, 20, 30, and 50 s) to deposit PtNPs. SEM images were taken to validate in the electrodeposition, as shown in **Figure 2**. Comparing Figure 2a–c, as the deposition time increases, PtNPs coverage of the graphene surface increases. The coverage percentage with respect to deposition

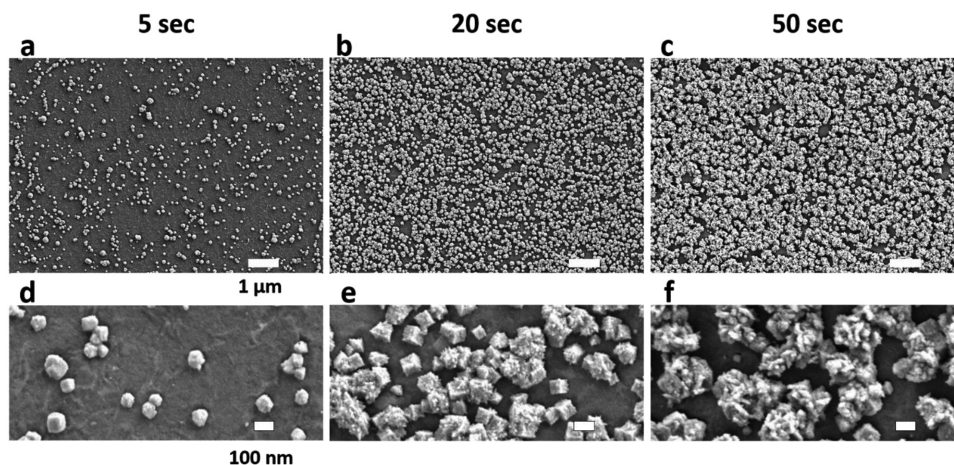


Figure 2. Scanning electron microscope images of PtNPs on graphene. a–c) show SEM images of PtNPs electrodeposited on graphene, the scale bar for these three panels is 1 μm . PtNPs cover 14.65%, 67.27%, and 88.22% of the graphene surface for 5, 20, 50 s depositions respectively. d–f) show SEM images at a higher magnification to point out the size and shape of the PtNPs. The size of PtNP is less than 100 nm for 5 s deposition, 100–200 nm for 20 s, and above 250 nm for 50 s. Further, the surface roughness of the PtNPs also increases with deposition time.

time is shown in Figure S5 (Supporting Information). The bottom row (Figure 2d–f) emphasizes the shape and size of the PtNPs. Diameters of PtNPs are mostly below 100 nm for 5 s deposition and above 250 nm for 50 s. 20 s deposition has some particles with 100 nm diameter, while the others \approx 200 nm. Similar trend applies for the surface roughness, longer deposition results in larger particle size and rougher surface. The size and surface roughness effect can be explained by the location of the reduction of PtCl_6^{2-} ions.^[17] If the reduction happens on graphene surface, it produces PtNPs with smooth surface and small size, as is the case for most PtNPs in 5 s deposition. If the reduction happens on an existing PtNP, it increases the surface roughness and the size, as is the case for most of the PtNPs in 50 s deposition.

The PtNPs/graphene electrodes were characterized with EIS and CV. EIS of PtNP/Graphene shows that the impedance significantly decreases as deposition time increases (Figure 3a). The impedances at 1 KHz are plotted as a function of deposition time including the impedance of the bare graphene microelectrodes in Figure 3b. PtNPs deposition achieves a 100-time decrease in the impedance. CV curves of PtNPs/Graphene electrodes show oxide reduction peaks at \approx –270 mV and hydrogen adsorption peaks at –900 to –400 mV (Figure 3c), all of which indicate that Pt is actively engaged in the charge-transfer process at electrode/electrolyte interface.^[17,19] As for simultaneous optical imaging or optogenetics experiments, high transmittance is equally important as the low impedance. We measured the optical transmittance spectra of PtNP/graphene microelectrodes with different deposition time at the wavelength range from 450 to 850 nm, as shown in Figure 3d. Monolayer graphene electrodes have an overall transmittance above 90%, and PtNP/Graphene electrodes with 30 s or less deposition time maintain a transparency above 50%, which is acceptable for simultaneous optical imaging and stimulation experiments.

Circuit models of electrode/electrolyte interface of Pt electrodes have been studied in detail in the literature.^[20] We modified equivalent circuit model for the graphene electrodes

(Figure 1d) to include the effect of PtNPs on the electrochemical interface. Since there are two types of materials, namely PtNPs and graphene, two circuit blocks for PtNPs and graphene respectively are constructed as shown in Figure 4a. In the PtNPs block, the infinite Warburg element (W_i) and the pseudo-capacitance (C_p) describing the pseudo-capacitor^[21] are needed to simulate how redox energy is stored at the PtNP surface. The parameters for the graphene block are calculated based on the fitting results from Table 1 and the surface coverage according to SEM images and then fixed in the model fitting; whereas solution resistance (R_s), Helmholtz double-layer capacitance (CPE_{pl}), W_i , and C_p for the PtNP block are obtained from fitting the model to the experimental results. Figure 4b,c demonstrates how the PtNP block (blue dashed curve) dominates the EIS characteristics over the graphene block (red dashed curve) for both 5 s and 50 s depositions, respectively. Even 5 s of electrodeposition causes PtNP block to dominate the total EIS over the graphene block, except at high frequency (above 40 KHz) where solution resistance (R_s) starts to be the dominant factor. This effect becomes more pronounced for 50 s deposition, where EIS of the Pt block is around two orders of magnitudes lower than that of the graphene block, so that the Pt dominates the characteristics of the electrode/electrolyte interface. These results suggest that the electrodeposition of PtNPs clearly overcomes the limitation of quantum capacitance of graphene and substantially decreases the total impedance. In addition to the EIS at open circuit potential, Figure 4d demonstrates the fitted pseudocapacitance with respect to the voltage bias at three different regions, namely hydrogen absorption, oxide reduction, and oxide formation, which are characteristic to Pt-based electrochemical interfaces. C_p increases as the voltage bias approaches the hydrogen absorption region, which is consistent with the electrochemical behavior of Pt electrodes reported previously.^[20] These results clearly demonstrate that PtNP deposition can overcome quantum capacitance limit of graphene electrodes by introducing a parallel redox path governed by electrochemical characteristics of Pt.

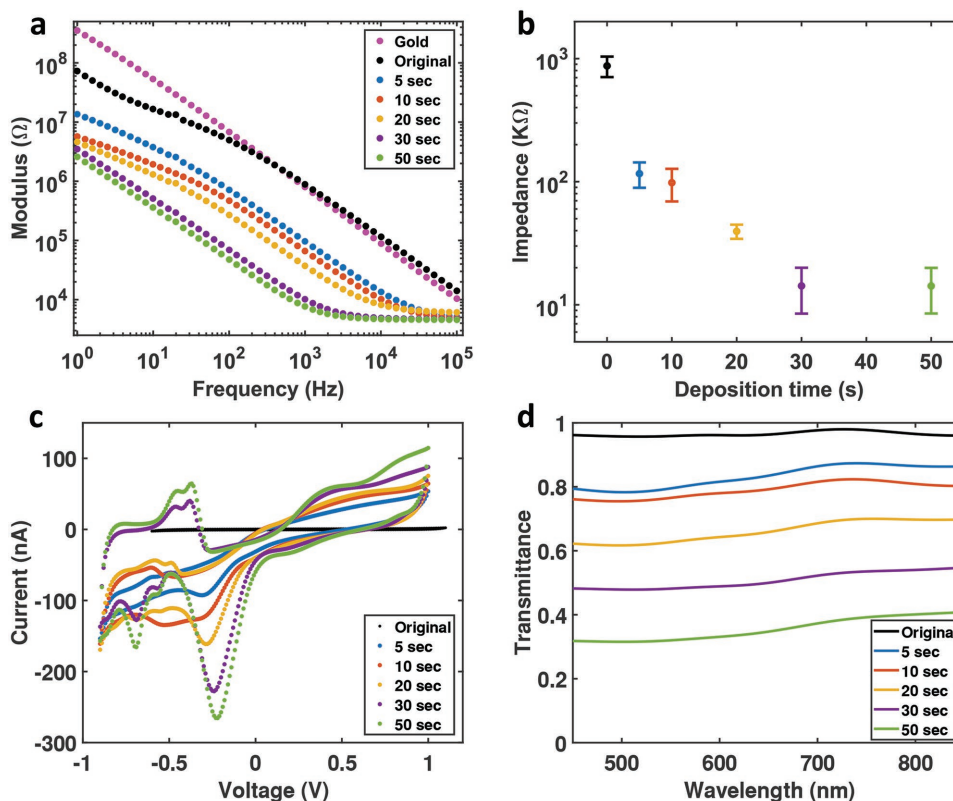


Figure 3. Characterization of PtNP/graphene electrodes. a) Electrochemical impedance spectroscopy of PtNP/graphene electrodes from 1 Hz to 100 KHz. The black dots are the impedance of the original graphene electrode (without PtNPs), the impedance of a gold electrode (magenta) is also plot for comparison. b) The impedance at 1 KHz has a clear trend to decrease with deposition time. c) Cyclic voltammetry of PtNP/graphene electrodes with a sweep rate of 200 mV s^{-1} . Bare graphene electrode without PtNPs (black) has no faradaic peaks, and the current is very small, and hence the curve looks like a straight line. As the deposition time increase, Faradaic peaks become more obvious, and the current gets higher. d) Transmittance spectra of PtNP/Graphene electrodes at wavelength from 450 to 850 nm.

2.3. Multimodal Monitoring of Cortical Potentials and Cellular Activity

We investigated whether PtNPs/graphene electrode cause obstruction of light penetration during optical imaging. Simultaneous *in vivo* two-photon calcium imaging and cortical field potential recordings were conducted in transgenic mouse models (cross between CaMKIIa-tTA^[22] and tetO-GCaMP6s^[23]). The PtNPs/graphene electrode array was placed on cortex centered at 2.2 mm posterior and 2.1 mm lateral relative to bregma, as shown in Figure 5a. Details about the surgery for implanting the transparent arrays above cortex and under optical imaging window are described in the Experimental Section. Two-photon imaging was performed at two depths, 50 and 250 μm to record signals from different sources. Dense neuropils, including axons and dendrites, were located at 50 μm (Movie S1, Supporting Information) while cell bodies of excitatory neurons were abundant at 250 μm (Movie S2 and S3, Supporting Information). Since there are no detected cell bodies at 50 μm , the main source of activity is the potential fluctuations in the neuropil. At 250 μm Ca^{2+} responses from cell bodies are clearly detectable (Figure 5b and Movie S3, Supporting Information). Gold wires (yellow dashed lines) connecting transparent graphene electrodes to recording amplifiers and active area of the electrodes (white dashed lines) where PtNPs were deposited are

outlined. Electrodes marked as A, B, C, and D in Figure 5b correspond to PtNPs deposition times of 10, 50, 5, and 5 s, respectively. Comparison of two-photon images directly beneath these electrodes suggests that PtNPs have no impact on the calcium imaging at 250 μm deep regardless of deposition time. Figure 5c is the maximum intensity projection of image stacks from 5 min record at Electrode B clearly showing cell bodies due to increased magnification. While opaque Au wires block the field of view and prevent imaging of the neurons directly beneath them, the neurons beneath the PtNP/graphene electrodes were clearly imaged with single-cell resolution at 250 μm depth due to the high transmittance of the electrodes. Figure S7 (Supporting Information) shows calcium imaging at five additional electrodes.

The calcium responses of four individual cells (highlighted in Figure 5c) are compared to illustrate the high transmittance of PtNP/graphene electrode. Cells 1 and 2 are directly beneath the PtNP/graphene electrode, Cells 3 and 4 do not overlap with PtNP/graphene area. To quantify the Ca^{2+} activities of these cells as shown in Figure 5d, we calculated $(F - F_0)/F_0$, where F is the mean fluorescence intensity of pixels under each electrode and F_0 is the 8th percentile of the intensity distribution for the entire recording session. Due to the high transmittance of PtNP/graphene electrode, calcium response of Cells 1 and 2 has a similar signal-to-noise ratio as Cells 3 and 4. These

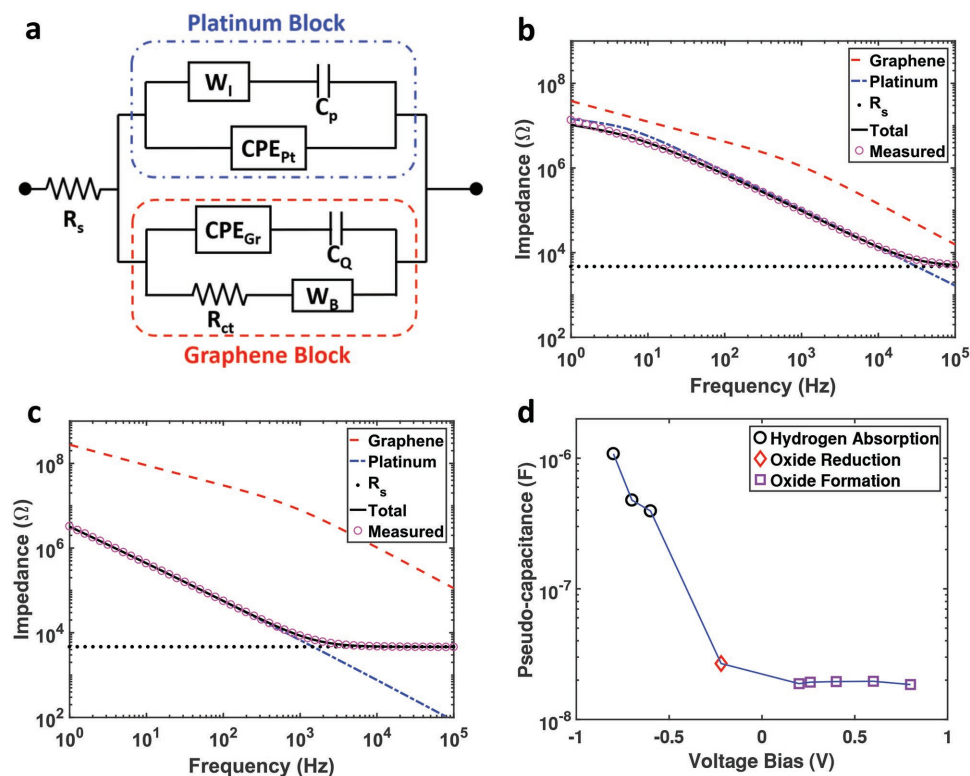


Figure 4. a) Equivalent circuit model contains two blocks for graphene and PtNPs, respectively. The parameters for the graphene block are fixed according to Table 1 and the coverage percentage according to SEM images. The PtNPs block and solution resistance (R_s) is obtained by fitting the measurement data to the circuit model. W_l , C_p , and CPE_{Pt} are the infinite Warburg element, pseudo-capacitance, and constant phase element for Pt double-layer capacitor respectively. b) Impedance of the graphene block (red dashed curve), Pt block (blue dashed curve) with respect to the total impedance of measurement (pink hollow circles) and fitting (black curve). The PtNPs block dominates the impedance over the graphene block at all frequencies. c) This effect is more obvious for 50 s deposition, except at frequencies above 40 KHz, where solution resistance starts to dominate. d) The fitted pseudocapacitance of 50 s deposition with respect to the voltage bias shows at the pseudocapacitance increases as the bias approaches hydrogen absorption region.

recordings confirm that PtNP/graphene electrodes do not obstruct deep calcium imaging directly beneath the electrodes.

The cortical potentials ($\mu ECoG$) and the spectrogram recorded by Electrode B are plotted in Figure 5e, synchronized with calcium responses in Figure 5d. $\mu ECoG$ recordings by Electrodes A, C, and D are shown in Figure S8 (Supporting Information). The $\mu ECoG$ shows spontaneous cortical activity recorded in awake animals without any distinct sensory stimulus. It includes contributions from both local and background neural activities. In that sense, similarity or correlation analysis cannot be directly applied to investigate contributions from different depths. Therefore, to further investigate the source of these surface potentials with respect to Ca^{2+} activities, we analyzed multimodal data consisting of Ca^{2+} spikes and $\mu ECoG$ potentials as explained in Figure 5g. The Ca^{2+} response is first smoothed by an eighth order Butterworth low-pass filter, and then a threshold is applied to find the time of each peaks. A 2 s time window prior to each Ca^{2+} peak is applied to the $\mu ECoG$ data, and the power within that time window across different frequency bands is obtained and converted to ratios. As is shown in Figure 5f, the power of ECoG oscillations prior to Ca^{2+} peaks at both depths have the same trend over a wide frequency range from δ to high- γ band. However, the power

ratios corresponding to Ca^{2+} signals at 50 μm are higher in the low-frequency band (δ and θ band) but lower at high-frequency band (γ and high- γ band), compared to those at 250 μm . This result suggests that synaptic activity from the neuropil mainly contributes to slower ECoG oscillations while spiking activity from cell bodies in deeper layers contributes to higher frequency bands such as γ and high- γ .

Application of transparent graphene microelectrode array technology in animal models combined with various optical techniques will pave the way towards better understanding of neural mechanisms underlying ECoG and electroencephalogram (EEG) signals. This is also important for clinical settings, as ECoG and EEG are often used in humans to indirectly infer underlying neural dynamics and disease mechanisms. The transparent nature of the current technology allows a combination with many existing optical technologies, including voltage imaging, optogenetics, wide-field imaging, in addition to two-photon calcium imaging demonstrated in this manuscript. Transparent graphene array implantation method can also be directly integrated with drug injection in the craniotomy, followed by implantation of the imaging windows. Drug injection procedure^[2b,24] is perfectly compatible with the transparent graphene ECoG array for pharmacological experiments.

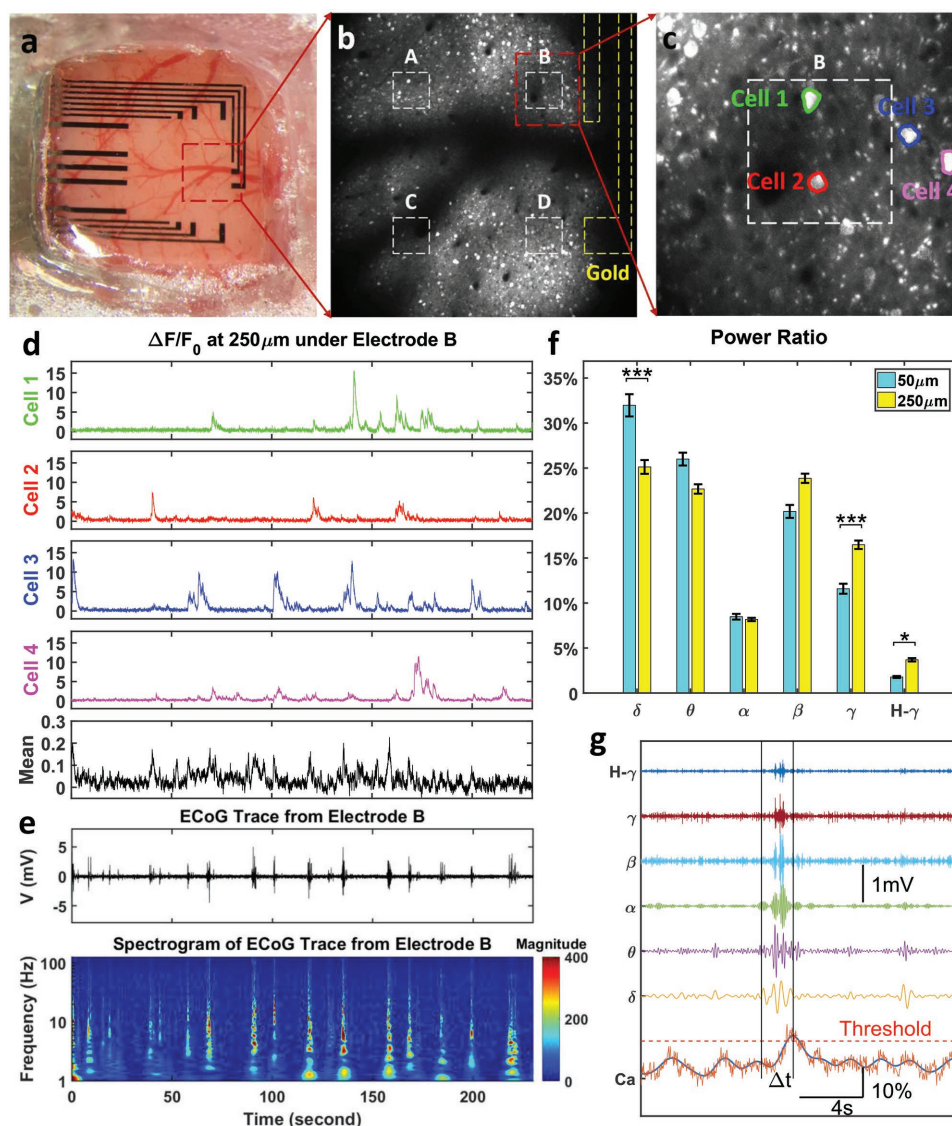


Figure 5. Simultaneous in vivo calcium imaging and ECoG recording. a) The PtNP/graphene electrode array was placed on the cortex centered at 2.2 mm posterior and 2.1 mm lateral relative to bregma. b) Two-photon microscope was focused at the depth of 250 μm from cortical surface to detect cell bodies, at the exact same location with 16 \times magnification. The deposition time for Electrodes A, B, C, and D is 10, 50, 5, and 5 s, respectively. c) Multiple cells can be clearly imaged, Cells 1 and 2 are directly under the PtNP/graphene electrode, and Cells 3 and 4 outside. The mean fluorescence change has a region of interest (ROI) the same as the electrode (white dashed box in Panel c). d) Fluorescence changes, e) ECoG trace, and the spectrogram were recorded and analyzed in a synchronized time frame. f) The power ratio of ECoG oscillations at 50 μm calcium peak time is larger in lower frequency range (delta band) and smaller in higher frequency range (gamma and high gamma bands) than at 250 μm . (Kruskal–Wallis test, $***p < 0.001$, $*p < 0.05$). g) The power of the ECoG oscillations at each calcium peak time was calculated at delta band (δ , 1–4 Hz), theta band (θ , 4–8 Hz), alpha band (α , 9–12 Hz), beta band (β , 13–30 Hz), gamma band (γ , 30–100 Hz), and high gamma band (H- γ , >100 Hz).

3. Conclusion

We demonstrated a novel microelectrode array with low impedance and high transmittance for simultaneous electrical recording and optical imaging of neural activity. PtNPs were electrodeposited on monolayer graphene to overcome the quantum capacitance limit and the lack of Faradaic reaction for the graphene electrodes. Equivalent circuit models for both graphene and PtNPs/graphene electrodes are developed to investigate how PtNPs serve as the redox catalyst at the electrode/electrolyte interface and how they decrease the electrochemical

impedance by 100 times. Furthermore, in vivo experiments with transgenic mice models validated that low impedance transparent graphene electrodes can be successfully employed for combining electrophysiology with optical imaging to support multimodal analysis that cannot be attainable using other approaches. Given the effectiveness of PtNP-electrodeposition, we envision that this technique is potentially applicable to fabricate transparent microelectrode arrays with various geometries specifically tailored toward probing different neural circuits and mechanism in multimodal experiments providing unprecedented spatiotemporal resolution.

4. Experimental Section

Graphene Transfer and Cleansing: In traditional transfer method, the metal substrate, copper in this case, was removed with wet-etching process.^[25] However, recent studies report copper etching leaves nanoscale copper residue and makes poly(methyl methacrylate) (PMMA) scaffold more difficult to be removed afterwards.^[26] Although the polymer residue is removable in H₂/Ar gas flow at above the decomposition temperature of PMMA (>200 °C),^[27] our PET substrate will lose its structure integrity starting at 150 °C. Therefore, to protect graphene from chemical contamination and mechanical damage, the “bubbling” transfer method^[10] was adopted with a 20 V DC power supply, and 0.05 M NaOH solution. Graphene was also doped in 35% nitric acid for 30 s as an effective way to increase charge carrier concentration during transfer (Figure S6, Supporting Information). After transfer, the sample needs to be dried completely at room temperature. The dried sample was then baked at 125 °C on a hotplate for 5 min to anneal PMMA wrinkles and enhance graphene/substrate bonding. PMMA can be removed by soaking the sample in acetone at room temperature for 20 min with gentle agitation. 10 cycles of IPA and DI water (1 minute each cycle each batch) is highly useful as mechanical cleansing.

Device Fabrication: The fabrication started with a 4 in. silicon wafer, cleaned, and dehydrated (Figure S1a, Supporting Information). 30 μm thick polydimethylsiloxane (PDMS) was spin-coated on the wafer and annealed at 150 °C for 10 min (Figure S1b, Supporting Information). This silicon wafer coated with PDMS was used as a holder to keep the PET substrate flat during the following processes. A 50 μm thick PET film was then placed on top of the PDMS layer (Figure S1c, Supporting Information). 10 nm chromium and 100 nm gold were sputtered onto the PET substrate with Denton Discovery 18 Sputter System (Figure S1d, Supporting Information). Metal wires and contact pads were patterned with photolithography and wet-etching (Gold Etchant TFA, Chromium Etchant 1020AC) (Figure S1e, Supporting Information). Monolayer graphene was transferred with the Experimental section described in detail above (Figure S1f, Supporting Information). To protect graphene from chemical and mechanical damage during photoresist removal, AZ1512/PMGI bilayer lithography is adopted: i) 100 nm PMGI SF3 is spin-coated at 3000 rpm for 45 s and soft-baked at 125 °C for 5 min; ii) 1.2 μm AZ1512 is spin-coated at 4000 rpm for 45 s and soft-baked at 100 °C for 1 min. The bilayer is then exposed with 135 mJ cm⁻² i-line UV and developed in AZ MIF 300. Graphene contact pads were patterned with oxygen plasma etching (Figure S1g, Supporting Information). Finally, the whole sample was encapsulated with 8 μm thick SU-8 2005 except openings at the designed regions (Figure S1h, Supporting Information). Gently peeled off from the PDMS/silicon wafer holder, the arrays (Figure S1i, Supporting Information) were ready for electrochemical characterizations.

Electrochemical Characterization: All electrochemical characterizations were performed with Gamry 600 Plus in 0.01 M phosphate buffered saline (Sigma-Aldrich P3813 dry powder dissolved in deionized water). Both EIS and CV were measured with a three-electrode configuration, where Ag/AgCl (gauge 25) and Pt (gauge 25) were used as a reference electrode and counter electrode, respectively. EIS were measured from 100 KHz to 1 Hz at open circuit potential unless otherwise stated. The AC voltage was 20 mV. CV was measured from -0.9 to 1 V versus Ag/AgCl for PtNP/graphene electrodes. 10 cycles of CV were measured to stabilize the electrode/electrolyte interface, and the tenth cycle was presented. To avoid electromagnetic noise, especially the 60 Hz one, the entire setup was placed inside of a Faraday cage.

Experimental Model and Subject Details: All procedures were in accordance with protocols approved by the UCSD Institutional Animal Care and Use Committee and the guidelines of the National Institutes of Health. Mice were obtained from The Jackson Laboratory (CaMKIIa-tTA: B6;CBA-Tg(Camk2a-tTA)1Mmay/J [JAX 003010]; tetO-GCaMP6s: B6;DBA-Tg(tetO-GCaMP6s)2Niell/J [JAX 024742]). Mice were typically group

housed with a reversed light cycle (12 h-12 h) in standard plastic disposable cages. Experiments were performed during the dark period.

Surgery: Adult mice (cross between CaMKIIa-tTA (JAX 003010)^[22] and tetO-GCaMP6s (JAX 024742),^[23] 2 months old) were anesthetized with isoflurane (3% for induction and 1% for maintenance) and a circular piece of scalp was removed. After cleaning the underlying bone using a razor blade, a custom-built head-post was implanted to the exposed skull (≈1 mm posterior to lambda) with cyanoacrylate glue and cemented with dental acrylic (Lang Dental). A stainless-steel screw (F000CE156, J.I. Morris) was implanted over cerebellum (≈0.5 mm posterior to lambda) as reference. A square craniotomy was made over the right hemisphere and the craniotomized area was 0–4.5 mm posterior and 0.3–4.0 mm lateral to bregma. The transparent PtNPs/graphene electrode array centered at 2.2 mm posterior and 2.1 mm lateral relative to bregma was placed on cortex. Cortical areas covered by the electrode array included primary somatosensory cortex (S1), posterior parietal cortex (PPC), primary visual cortex (V1), and secondary visual cortex (V2). An imaging window consisting of a glass plug glued on to a larger glass base was placed on top of the electrode array. 3% agarose was applied to fill the gap between the skull and the window and the window was further secured with vetbond (3M) and dental acrylic. A cocktail of dexamethasone (2 mg per kg body weight), buprenorphine (0.1 mg per kg body weight), and buprenorphine (10 mg per kg body weight) was given at the end of surgery. The animal was returned to the home cage and fully recovered from anesthesia before recording.

In Vivo calcium imaging: Two-photon imaging was conducted for a head-fixed awake mouse through a 16 × 0.8 NA objective (Nikon) mounted on a commercial two-photon microscope (B-scope, Thorlabs) and using a 925 nm laser (Ti:sapphire laser, Newport). Images were acquired at ≈29 Hz and a resolution of 512 × 512 pixels, covering either 944 × 1016 μm (Figure 5b) or 189 × 203 μm (Figure 5c). Acquired images were motion corrected offline. For quantification of Ca²⁺ signals from cell bodies, fluorescence time course of each cellular ROI and its surrounding neuropil ROI was extracted using Suite2P package. Then fluorescence signal of a cell body was estimated with $F_{\text{cellbody}} = F_{\text{cellROI}} - 0.7 * F_{\text{neuropilROI}}$ as described previously.^[28] $\Delta F/F$ was computed as $(F_{\text{cellbody}} - F_0)/F_0$, where F_0 is the 8th percentile of the intensity distribution during 5 min recording session. For quantification of Ca²⁺ signals at the depth of 50 and 250 μm, ROIs along the edges of each electrode were drawn.

Supporting Information

Supporting Information is available from the Wiley Online Library or from the author.

Acknowledgements

The authors acknowledge Office of Naval Research Young Investigator Award (N00014161253), National Science Foundation (ECCS-1752241, ECCS-1734940), San Diego Frontiers of Innovation Scholars Program, Kavli Institute for Brain and Mind Innovative Research, and NIH (R01 NS091010A, R01 EY025349, R01 DC014690, U01 NS094342, P30EY022589) for funding this research. This work was performed in part at the San Diego Nanotechnology Infrastructure (SDNI) of UCSD, a member of the National Nanotechnology Coordinated Infrastructure, which is supported by the National Science Foundation (Grant ECCS-1542148).

Conflict of Interest

The authors declare no conflict of interest.

Keywords

calcium imaging, electrocorticography, graphene, platinum nanoparticles, quantum capacitance

Received: January 1, 2018

Revised: March 25, 2018

Published online: June 5, 2018

- [1] a) G. Buzsáki, C. A. Anastassiou, C. Koch, *Nat. Rev. Neurosci.* **2012**, *13*, 407; b) G. Buzsáki, *Nat. Neurosci.* **2004**, *7*, 446.
- [2] a) T. Komiyama, T. R. Sato, D. H. O'Connor, Y.-X. Zhang, D. Huber, B. M. Hooks, M. Gabitto, K. Svoboda, *Nature* **2012**, *464*, 1182; b) A. J. Peters, S. X. Chen, T. Komiyama, *Nature* **2014**, *510*, 263; c) A. Allalou, Y. Wu, M. Ghannad-Rezaie, P. M. Eimon, M. F. Yanik, *eLife* **2017**, *6*, e23379; d) D. Vallentin, G. Kosche, D. Lipkind, M. A. Long, *Science* **2016**, *351*, 267.
- [3] a) A. Badura, X. N. R. Sun, A. Giovannucci, L. A. Lynch, S. S. H. Wang, *Neurophotonics* **2014**, *1*, 025008; b) C. Stosiek, O. Garaschuk, K. Holthoff, A. Konnerth, *Proc. Natl. Acad. Sci. USA* **2003**, *100*, 7319.
- [4] a) D. Kuzum, H. Takano, E. Shim, J. C. Reed, H. Juul, A. G. Richardson, J. De Vries, H. Bink, M. A. Dichter, T. H. Lucas, *Nat. Commun.* **2014**, *5*, 6259; b) D. W. Park, A. A. Schendel, S. Mikael, S. K. Brodnick, T. J. Richner, J. P. Ness, M. R. Hayat, F. Atry, S. T. Frye, R. Pashaie, S. Thongpang, Z. Q. Ma, J. C. Williams, *Nat. Commun.* **2014**, *5*, 5258; c) K. Kostarelos, M. Vincent, C. Hebert, J. A. Garrido, *Adv. Mater.* **2017**, *29*, 1700909.
- [5] a) M.-H. Bae, Z. Li, Z. Aksamija, P. N. Martin, F. Xiong, Z.-Y. Ong, I. Knezevic, E. Pop, *Nat. Commun.* **2013**, *4*, 1734; b) H.-S. P. Wong, D. Akinwande, *Carbon Nanotube and Graphene Device Physics*, Cambridge University Press, New York **2011**; c) D. Akinwande, N. Petrone, J. Hone, *Nat. Commun.* **2014**, *5*, 5678; d) L. Tao, J. Lee, H. Chou, M. Holt, R. S. Ruoff, D. Akinwande, *ACS Nano* **2012**, *6*, 2319; e) S. Lee, J. Sohn, Z. Jiang, H.-Y. Chen, H.-S. P. Wong, *Nat. Commun.* **2015**, *6*, 8407; f) K. L. Grosse, M.-H. Bae, F. Lian, E. Pop, W. P. King, *Nat. Nanotechnol.* **2011**, *6*, 287; g) H. Y. Park, W. S. Jung, D. H. Kang, J. Jeon, G. Yoo, Y. Park, J. Lee, Y. H. Jang, J. Lee, S. Park, *Adv. Mater.* **2016**, *28*, 864.
- [6] a) B. M. Venkatesan, D. Estrada, S. Banerjee, X. Jin, V. E. Dorgan, M.-H. Bae, N. R. Aluru, E. Pop, R. Bashir, *ACS Nano* **2011**, *6*, 441; b) F. Schedin, A. Geim, S. Morozov, E. Hill, P. Blake, M. Katsnelson, K. Novoselov, *Nat. Mater.* **2007**, *6*, 652.
- [7] a) L. D'Arise, S. Esconjauregui, R. S. Weatherup, X. Y. Wu, W. E. Arter, H. Sugime, C. Cepek, J. Robertson, *RSC Adv* **2016**, *6*, 113185; b) A. Kasry, M. A. Kuroda, G. J. Martyna, G. S. Tulevski, A. A. Bol, *ACS Nano* **2010**, *4*, 3839.
- [8] a) P. Ledochowitsch, E. Olivero, T. Blanche, M. M. Maharbiz, presented at Engineering in Medicine and Biology Society, EMBC, 2011 Annual Int. Conf. of the IEEE, Boston, MA, USA, December, **2011**; b) K. Y. Kwon, B. Sirowatka, A. Weber, W. Li, *IEEE Trans. Biomed. Circuits Syst.* **2013**, *7*, 593.
- [9] T. Fang, A. Konar, H. L. Xing, D. Jena, *Appl. Phys. Lett.* **2007**, *91*, 092109.
- [10] Y. Wang, Y. Zheng, X. F. Xu, E. Dubuisson, Q. L. Bao, J. Lu, K. P. Loh, *ACS Nano* **2011**, *5*, 9927.
- [11] W. Franks, I. Schenker, P. Schmutz, A. Hierlemann, *IEEE Trans. Biomed. Eng.* **2005**, *52*, 1295.
- [12] A. Hassibi, R. Navid, R. W. Dutton, T. H. Lee, *J. Appl. Phys.* **2004**, *96*, 1074.
- [13] a) E. Uesugi, H. Goto, R. Eguchi, A. Fujiwara, Y. Kubozono, *Sci. Rep.* **2013**, *3*, 1595; b) H. X. Ji, X. Zhao, Z. H. Qiao, J. Jung, Y. W. Zhu, Y. L. Lu, L. L. Zhang, A. H. MacDonald, R. S. Ruoff, *Nat. Commun.* **2014**, *5*, 3317; c) J. L. Xia, F. Chen, J. H. Li, N. J. Tao, *Nat. Nanotechnol.* **2009**, *4*, 505.
- [14] C. Zhan, J. Neal, J. Z. Wu, D. E. Jiang, *J. Phys. Chem. C* **2015**, *119*, 22297.
- [15] a) Y. G. Zhou, J. J. Chen, F. B. Wang, Z. H. Sheng, X. H. Xia, *Chem. Commun.* **2010**, *46*, 5951; b) Y. J. Hu, H. Zhang, P. Wu, H. Zhang, B. Zhou, C. X. Cai, *Phys. Chem. Chem. Phys.* **2011**, *13*, 4083; c) Y. J. Li, W. Gao, L. J. Ci, C. M. Wang, P. M. Ajayan, *Carbon* **2010**, *48*, 1124.
- [16] H. Wu, J. Wang, X. H. Kang, C. M. Wang, D. H. Wang, J. Liu, I. A. Aksay, Y. H. Lin, *Talanta* **2009**, *80*, 403.
- [17] D. Zhang, W. C. Chang, T. Okajima, T. Ohsaka, *Langmuir* **2011**, *27*, 14662.
- [18] S. Singal, A. Biradar, A. Mulchandani, *Appl. Biochem. Biotechnol.* **2014**, *174*, 971.
- [19] a) E. M. Hudak, D. Kumsa, H. Martin, J. Mortimer, *J. Neural Eng.* **2017**, *14*, 046012; b) P. Daubinger, J. Kieninger, T. Unmussig, G. A. Urban, *Phys. Chem. Chem. Phys.* **2014**, *16*, 8392.
- [20] H. D. Yoo, J. H. Jang, B. H. Ka, C. K. Rhee, S. M. Oh, *Langmuir* **2009**, *25*, 11947.
- [21] D. R. Merrill, M. Bikson, J. G. R. Jefferys, *J. Neurosci. Methods* **2005**, *141*, 171.
- [22] M. Mayford, M. E. Bach, Y.-Y. Huang, L. Wang, *Science* **1996**, *274*, 1678.
- [23] J. B. Wekselblatt, E. D. Flister, D. M. Piscopo, C. M. Niell, *J. Neurophysiol.* **2016**, *115*, 2852.
- [24] a) H. Makino, C. Ren, H. X. Liu, A. N. Kim, N. Kondapaneni, X. Liu, D. Kuzum, T. Komiyama, *Neuroendocrinology* **2017**, *94*, 880; b) H. Makino, T. Komiyama, *Nat. Neurosci.* **2015**, *18*, 1116.
- [25] a) M. Her, R. Beams, L. Novotny, *Phys. Lett. A* **2013**, *377*, 1455; b) J. D. Wood, G. P. Doidge, E. A. Carrion, J. C. Koepke, J. A. Kaitz, I. Datye, A. Behnam, J. Hewaparakrama, B. Aruin, Y. F. Chen, H. Dong, R. T. Haasch, J. W. Lyding, E. Pop, *Nanotechnology* **2015**, *26*, 055302; c) T. Matsumae, A. D. Koehler, T. Suga, K. D. Hobart, *J. Electrochem. Soc.* **2016**, *163*, E159.
- [26] Y. C. Lin, C. C. Lu, C. H. Yeh, C. H. Jin, K. Suenaga, P. W. Chiu, *Nano Lett.* **2012**, *12*, 414.
- [27] A. Pirkle, J. Chan, A. Venugopal, D. Hinojos, C. Magnuson, S. McDonnell, L. Colombo, E. Vogel, R. Ruoff, R. Wallace, *Appl. Phys. Lett.* **2011**, *99*, 122108.
- [28] a) T. W. Chen, T. J. Wardill, Y. Sun, S. R. Pulver, S. L. Renninger, A. Baohan, E. R. Schreier, R. A. Kerr, M. B. Orger, V. Jayaraman, L. L. Looger, K. Svoboda, D. S. Kim, *Nature* **2013**, *499*, 295; b) M. Pachitariu, C. Stringer, S. Schröder, M. Dipoppa, L. F. Rossi, M. Carandini, K. D. Harris, *BioRxiv* **2016**, 061507.